(left margin, repeated)

HHS Public Access

Seeing Through the Surface: Non-Invasive Characterization of Biomaterial-Tissue Interactions Using Photoacoustic Microscopy

Yu Shrike Zhang[1,2,3], **Lihong V. Wang**[4,*], and **Younan Xia**[5,6,*]

[1]Biomaterials Innovation Research Center, Department of Medicine, Brigham and Women's Hospital, Harvard Medical School, Boston, MA 02115, USA

[2]Harvard-MIT Division of Health Sciences and Technology, Massachusetts Institute of Technology, Cambridge, MA 02139, USA

[3]Wyss Institute for Biologically Inspired Engineering, Harvard University, Boston, MA 02115, USA

[4]Department of Biomedical Engineering, Washington University in St. Louis, St. Louis, MO 63130, USA

[5]The Wallace H. Coulter Department of Biomedical Engineering, Georgia Institute of Technology and Emory University, Atlanta, GA 30332, USA

[6]School of Chemistry and Biochemistry, School of Chemical and Biomolecular Engineering, Georgia Institute of Technology, Atlanta, GA 30332, USA

Abstract

At the intersection of life sciences, materials science, engineering, and medicine, regenerative medicine stands out as a rapidly progressing field that aims at retaining, restoring, or augmenting tissue/organ functions to promote the human welfare. While the field has witnessed tremendous advancements over the past few decades, it still faces many challenges. For example, it has been difficult to visualize, monitor, and assess the functions of the engineered tissue/organ constructs, particularly when three-dimensional (3D) scaffolds are involved. Conventional approaches based on histology are invasive and therefore only convey end-point assays. The development of volumetric imaging techniques such as confocal and ultrasonic imaging has enabled direct observation of intact constructs without the need of sectioning. However, the capability of these techniques is often limited in terms of penetration depth and contrast. In comparison, the recently developed photoacoustic microscopy (PAM) has allowed us to address these issues by integrating optical and ultrasonic imaging to greatly reduce the effect of tissue scattering of photons with one-way ultrasound detection while retaining the high optical absorption contrast. PAM has been successfully applied to a number of studies, such as observation of cell distribution, monitoring of vascularization, and interrogation of biomaterial degradation. In this review article, we highlight

*Corresponding authors: Younan Xia, Ph.D. The Wallace H. Coulter Department of Biomedical Engineering, Georgia, Institute of Technology and Emory University, Atlanta, Georgia 30332, USA. Telephone: +1 404 385 3209, fax: +1 404 894 4243, younan.xia@bme.gatech.edu; Lihong V. Wang, Ph.D., Department of Biomedical Engineering, Washington University in St. Louis, St. Louis, MO 63130, USA. Telephone: +1 314 935 6152, fax: +1 314 935 7448, lhwang@wustl.edu.

all other authors declare no conflict of interest.

recent progress in non-invasive and volumetric characterization of biomaterial-tissue interactions using PAM. We also discuss challenges ahead and envision future directions.

Keywords

Photoacoustic microscopy; biomedical imaging; tissue engineering; regenerative medicine; non-invasive

Introduction

Regenerative medicine aims to create functional tissues/organs to replace those damaged or diseased in the body by using an interdisciplinary approach involving materials science, engineering, cell biology, and medicine.[1] The materials, typically processed as three-dimensional (3D) scaffolds containing well-defined structures and architecture, play a pivotal role in tissue regeneration by functioning as biomimetic substrates for cells to reside, respond, and remodel.[2, 3] The scaffolds, when formed in different shapes, architecture, porosities, interconnectivity, and degradation profiles, can be rendered to fit for desired applications.[2-5] Functionalization of the scaffolds with bioactive molecules further endows these biomimetic matrices with extended capability to precisely manipulate cellular behaviors for the formation of functional tissues.[2, 3]

In evaluating the efficacy of these approaches to promote tissue regeneration, it is necessary to assess a number of properties of the engineered tissue constructs, such as the viability, distribution, and proliferation of cells; the production/spatial arrangement of extracellular matrix, and degradation of the scaffold. However, it has always been a challenge to characterize 3D biological samples in a non-invasive and chronological manner. Conventional methods based on microtomy, where serial sections are obtained from a sample, are laborious and the capability to reconstruct the volumetric information is rather limited.[6] In addition, the requirement of sectioning is destructive, which does not allow for repeated measurements of the same sample over an extended period of time. The use of multiple samples would increase the probability of errors originating from variations in scaffold and tissue fabrication. To this end, non-invasive, volumetric imaging modalities have clear advantages over the invasive methods.[7, 8] Although many potent imaging technologies have been developed over the past years, limitations persist. For example, while pure optical imaging modules such as confocal and multi-photon microscopy can achieve high resolution,[9] their penetration depths are usually confined to no more than a few hundred micrometers due to strong optical scattering of biological tissues.[10] On the other hand, non-optical imaging modalities such as ultrasound,[11] micro-computed tomography (micro-CT),[12] magnetic resonance imaging (MRI),[13] and positron emission tomography (PET)[14] are capable of deep imaging, but they are plagued by relatively low resolution, slow response, and/or ionizing irradiation. None of these existing imaging techniques can meet the pressing needs of characterizing engineered tissues for regenerative medicine.

Photoacoustic microscopy, or PAM, is a recently developed volumetric imaging modality that elegantly combines optical with ultrasonic imaging to achieve both high resolution arising from the optical absorption contrast as well as deep penetration of up to multiple

millimeters due to the low scattering of acoustic waves by biological tissues.[7, 15-23] Since its invention, PAM has been widely adopted for a variety of biomedical and medical applications ranging from the characterization of subcellular organelles and cells all the way to tissues and organs. For example, melanomas[24, 25] and blood vessels[16, 26] can be directly imaged by PAM in preclinical models without the need of external contrasts because of their intrinsic pigmentation, with melanin for melanoma cells and hemoglobin for erythrocytes, respectively. The great resolution and penetration depth of PAM have particularly rendered such modality useful for characterizing tissue-biomaterial interactions on the right scale.[7] In this review, we first introduce the principle of PAM and discuss its suitability in imaging engineered tissue constructs. We then continue to present examples where PAM has been successfully applied to monitoring subcellular responses, cells, scaffolds, vasculature, and the interactions among these components. Finally we conclude with future perspectives on maximizing the utility of PAM for applications in tissue engineering or regenerative medicine.

Photoacoustic Microscopy

PAM relies on the optical absorption contrast to image specimens. In PAM, both the optical excitation and the ultrasonic detection are focused, where the foci are configured coaxially and confocally.[17, 20] Upon illumination of an optically absorbing object with a pulsed or intensity-modulated laser, the transient thermoelastic expansion and contraction of the sample will produce acoustic waves. For each single-point laser shot, time-resolved ultrasonic detection produces a one-dimensional (1D), depth-resolved image. Thus, a 1D line scan produces a two-dimensional (2D) frame, and a 2D raster scan along the transverse plane generates complete 3D data. Volumetric data can be viewed through projection images coded by either amplitude of maximum (*i.e.*, maximum amplitude projection, MAP) or depth of maximum, or direct 3D rendering. Typically, PAM can be used for imaging at a millimeter scale in terms of depth, together with micrometer-scale resolution. The axial resolution and the maximum penetration depth are dependent on the central frequency of the ultrasonic transducer, while the lateral resolution is predominantly determined by the tighter focus of the dual optical-ultrasonic foci.[7, 17, 20]

PAM systems commonly used for regenerative medicine applications can be classified into optical-resolution PAM (OR-PAM) and acoustic-resolution PAM (AR-PAM) according to the resolution.[7, 17, 20] Figure 1a shows a schematic of OR-PAM,[20, 27] where a bright-field optical illumination, with a much tighter focus than the acoustic focus, is adopted to achieve optical resolution. The pulses from the laser are focused by a microscope objective into the sample. The generated photoacoustic signals are detected by a focused ultrasonic transducer, which is placed confocally with the objective. The optical focal spot size of <5 μm is much smaller in diameter than the acoustic focus, so the lateral resolution is mainly determined by the optical focal spot size to achieve the so-called "optical resolution". The OR-PAM generally has a lateral resolution finer than 5 μm, which is dependent on the optical wavelength and the numerical aperture (NA) of the objective,[24, 27] and a penetration depth of up to 1.2 mm in soft tissues.[27]

A schematic of AR-PAM is shown in Figure 1b.[16, 20] The excitation is implemented through a dark-field illumination, and the light is reshaped by a conical lens to form a ring pattern. The ring-shaped light is then weakly focused into the sample by an optical condenser. The generated photoacoustic signals are detected using a focused ultrasonic transducer located in the center of the optical condenser. The optical and ultrasonic foci are configured coaxially and confocally. The optical focal spot size is on the millimeter scale in diameter, much larger than the ultrasonic focus, and therefore the lateral resolution is predominantly determined by the ultrasonic focus, the so-called "acoustic resolution". The AR-PAM can achieve a lateral resolution of approximately 45 μm, an axial resolution of approximately 15 μm, and a penetration depth of more than 3 mm in soft tissues.[16]

It should be noted that the light in OR-PAM may experience multiple scattering events before reaching the focal point in biological tissues. While the lateral resolution of PAM is the finest at the depth corresponding to the focus of the objective for OR-PAM or the ultrasonic transducer for AR-PAM, the resolution deteriorates as a function of distance away from the focal point. In order to maintain the high resolution of PAM over an extended depth range, depth scanning may further be implemented besides raster scanning at the expense of imaging speed.[28, 29] Additionally, limited-diffracting Bessel beams can be used to extend the focal zone for OR-PAM,[29, 30] whereas synthetic-aperture focusing technique based on a virtual-detector in combination with coherence weighting may be adopted for AR-PAM.[29, 31, 32]

Figure 1c graphically illustrates the correlation between the imaging depth and spatial resolution of PAM. The acoustic nature of photoacoustic imaging allows it to easily achieve a high depth-to-resolution ratio of roughly 200, constant across all PAM modalities.[17, 20] The optimal tradeoff between spatial resolution and imaging depth should depend on the specific application of PAM. Indeed, PAM and its extended forms, photoacoustic macroscopy (PAMac) and photoacoustic computed tomography (PACT),[33, 34] have been used to probe biological structures across multiple scales,[17, 20, 35] from subcellular imaging of individual melanosomes (Fig. 1d),[24] functional imaging of individual red blood cells flowing in capillaries (Fig. 1e),[36] and diagnosis of human skin lesions (Fig. 1f),[37] all the way to clinical imaging of the breast vasculature in a human subject (Fig. 1g).[38]

While PAM provides superb contrast from optical absorption, hybrid systems integrating PAM with other modalities have also been constructed to increase its capability. For example, OR-PAM has been complemented with both fluorescence confocal microscopy (OR-PAM-FCM)[39] and optical coherence tomography (OR-PAM-OCT).[40] In OR-PAM-FCM, a dichroic mirror and an emission filter of desired wavelength allows the transmission of fluorescence emitted from the sample for generating the image. The FCM subsystem has a lateral resolution of approximately 3.9 μm, an axial resolution of about 38 μm, and a penetration depth of roughly 1 mm in soft tissues.[39] In OR-PAM-OCT, the OCT subsystem measures the depth-resolved backscattered light from the object. The OCT subsystem has a lateral resolution of about 5 μm and an axial resolution of about 5.9 μm in soft tissues; the axial imaging range of OCT is roughly 2 mm in soft tissues.[40]

PAM Imaging of Cells

As the most fundamental biological component, cells actively respond to and remodel the local microenvironment in the development of engineered tissues. Therefore, the ability to characterize the cells in a tissue construct becomes a critical step towards the widespread applications of PAM in regenerative medicine. While early examples were demonstrated by the use of melanoma cells that contain natural dark pigments melanin with optical absorption across the visible and near infrared (NIR) regions, recent advances have also shifted to genetic engineering and staining by exogenous contrast agents to render essentially all types of cells with proper contrast mechanisms for PAM imaging.[41, 42]

Melanoma cells

Melanoma cells are a type of skin cancer cells that contain melanosomes with residing melanin, a natural dark pigment. Consequently, melanoma cells are black in color due to the strong optical absorption of melanin in the UV-visible-NIR regions, rendering them conveniently measureable by PAM.[24, 25] The feasibility of non-invasive 3D imaging of melanoma cells in biomaterial scaffolds was initially demonstrated by us using AR-PAM.[43] The PAM coronal and sagittal MAP images in Figure 2a clearly show the distribution of melanoma cells in a poly(lactic-*co*-glycolic acid) PLGA inverse opal scaffold with a thickness of 1.5 mm. The volumetric data could also be directly rendered by 3D depiction (Fig. 2b), where individual melanoma cells or cell clusters could be mapped relative to the position of the scaffold. At a lateral resolution of 45 μm, it is rather fascinating to have a penetration depth of a few millimeters for AR-PAM, which covers the thickness range of the majority of the engineered tissue constructs. On the contrary, a confocal or multi-photon microscope could only reach a depth of several hundred micrometers at the maximum, due to the pronounced optical scattering by both the scaffold and the embedded cellular/extracellular components.[7]

More interestingly, it has been shown that AR-PAM could further be used to temporally monitor and quantify cell proliferation in individual scaffolds at relatively high spatial resolution. Such a capacity is highly desired since conventional methods based on imaging multiple samples at different time points cannot retrieve information of a single construct over time. Figure 2c reveals time-series PAM coronal MAP images of melanoma cells in the same scaffold up to 14 days, where the increase in the number of cells could be readily observed. The volumetric data obtained using PAM was quantifiable based on the intensity of measured signals, and the quantification results matched those derived from the biochemical 3-(4,5-dimethylthiazol-2-yl)-2,5-diphenyltetrazolium (MTT) assay (Fig. 2d). Since the laser fluence may vary during raster scanning, the absolute photoacoustic signal of each voxel has to be normalized against the corresponding laser fluence in order to achieve accurate quantification.

Genetically engineered cells

In order to achieve PAM imaging of non-pigmented cells, researchers have devised a variety of approaches based on genetically engineering the cells to introduce intrinsic contrast mechanisms. Among all, fluorescent proteins have evolved as one of the most commonly

used techniques for optical imaging, where cells can be engineered to express these proteins of desired optical properties and under different promoters to allow for functional imaging of subcellular events.[44] While a higher quantum yield gives better imaging quality for optical microscopy, fluorescent proteins with lower quantum yields would elicit more efficient photothermal conversion that is better suited for PAM measurement.[41, 42, 45] Taking advantages of such concept, Verkhusha, Wang, and co-workers demonstrated that red fluorescent proteins (RFPs) with distinctive absorption peaks in the NIR region allowed for convenient PAM imaging (Fig. 3, a and b).[46, 47] The differential absorption spectra of the RFP subtypes further enabled PAM with a capability to un-mix them at deep depth (Fig. 3c). Cells expressing these RFPs could be imaged both *in vitro* and *in vivo* using PAM at high resolution and deep penetration depth.

More recently, researchers have developed an approach to transfect cells with genes encoding tyrosinase, which could oxidize tyrosine to the dark pigment melanin through a chain of intracellular reactions (Fig. 3d).[48] In this case, the introduction of tyrosinase into target cells forces them to produce the absorption contrast for PAM imaging.[49, 50] Unlike fluorescent proteins, the melanin produced by the cells has properties similar to those present in the melanoma cells, meaning that it possesses a constant strong absorption across the visible and NIR ranges (Fig. 3e).[50] Both the Wang and Beard Groups showed that, HEK 293 cells transfected with tyrosinase induced the cells to express melanin,[49, 50] as revealed in transmission electron microscopy (TEM) images (Fig. 3f) and optical micrographs (Fig. 3g). The 293-tyrosinase cells, when observed under PAM, exhibited strong signals comparable to the B16 melanoma cells, whereas the wild type cells could not be imaged (Fig. 3h).

The LacZ/β-galactosidase reporter gene system is another long-standing technique for measuring successful gene transfection.[51] Cells carrying such reporter gene will produce β-galactosidase, which catalyzes the hydrolysis of 5-bromo-4-chloro-3-indolyl-β-D-galactopyranoside (X-gal) into galactose and 5-bromo-4-chloro-3-hydroxyindole; the latter molecule then spontaneously dimerizes and is subsequently oxidized into 5,5′-dibromo-4,4′-dichloro-indigo, a blue precipitate that is water insoluble (Fig. 3i).[52] The 5,5′-dibromo-4,4′-dichloro-indigo has a strong absorption in the visible light regime that is distinctive from that of the blood (Fig. 3j),[53, 54] consequently allowing for efficient PAM imaging. Figure 3k shows an OR-PAM image and an optical image of the 9L/LacZ glioblastoma cells stained with X-gal.[55] After staining the blue precipitations of 5,5′-dibromo-4,45′-dichloro-indigo were clearly discernible under PAM. Although X-gal is the most commonly used substrate for β-galactosidase, there are many variants that produce other colors after hydrolysis, such as 5-bromo-3-indolyl-β-D-galactopyranoside (dark blue), N-methylindolyl-β-D-galactopyranoside (green), 6-chloro-3-indolyl-β-D-galactopyranoside (pink), 5-bromo-6-chloro-3-indolyl-β-D-glucopyranoside (magenta), and 5-iodo-3-indolyl-β-D-galactopyranoside (purple).[52] These different substrates potentially enable a greater choice over the spectral regions in which PAM can be used for imaging cells engineered with the LacZ reporter system.

Contrast agent-stained cells

Contrast enhancement enabled by chemical staining has also been widely adopted for PAM imaging of cells and subcellular structures.[41, 42] Comparing to genetic engineering, approaches based on exogenous contrast agents are in general faster and more conveniently available to researchers. To this end, several contrasting mechanisms based on chemicals and nanoparticles have been adopted and demonstrated.

We demonstrated that, MTT, a tetrazole that is reduced to MTT formazan in living cells, could be used as a strong contrast agent for PAM.[56] The MTT assay has long been used to biochemically evaluate the metabolic activity of cells.[57] The MTT is water-soluble and has a yellowish color only with absorption below 450 nm. By contrast, MTT formazan is insoluble in water; the crystals have a strong absorption in the spectral region of 500–700 nm and a peak at around 650 nm. As a result, the formazan generated inside living cells can be directly used to enhance their contrast for PAM, where the crystals functions as an equivalent to the natural pigments in melanoma cells.[56]

Using MTT formazan as a contrast agent, we have successfully demonstrated that non-pigmented cells could be imaged under PAM at a contrast proportional to the amount of formazan formed inside the cells.[56] It was found that, such staining method is universal, and can be applied to all cell types that are metabolically active. We further proved the feasibility of PAM for 3D imaging of cells after staining with MTT formazan. As shown in Figure 4a, AR-PAM could obtain volumetric information of the distribution of MC3T3 preosteoblasts cultured in an inverse opal scaffold after 3 h of incubation in a medium containing 5 mg/mL MTT, with the capability of 3D rendering (Fig. 4b), indicating the efficacy of the contrast provided by MTT formazan. Even when embedded in an alginate hydrogel inside a scaffold, MTT molecules could still diffuse and stain the cells (Fig. 4c). Comparison between PAM and optical microscopy images clearly showed matching features between the two (Fig. 4d). Again, the proliferation of the cells inside a scaffold was quantifiable, and comparable to the biochemical MTT analysis (Fig. 4, e and f). A cell invasion assay was further performed, where inward proliferation of cells from the surface of the inverse opal scaffolds could be observed (Fig. 4g). With the non-invasively quantification of cell migration depth using PAM, the differential rates of cell migration into the scaffolds with two set of pore sizes could be calculated (Fig. 4h).

Besides MTT formazan, it should be noted that other tetrazolium-formazan systems, which possess absorption peaks covering spectral ranges different from MTT formazan, could also be used.[57] Together, these various tetrazolium-formazan systems will potentially enable multi-wavelength imaging of cells and engineered biological structures by PAM.

Another strategy for staining the cells for PAM imaging is based on the chromogenic (immune)cytochemistry. Although such a staining method has been used as a pivotal tool for cell biology, pathology, and medicine for a century, its capacity is limited by the conventional optical microscopy in that only a very thin layer of tissues, typically in the sub-10-μm thickness, can be examined at a time. Consequently, the traditional histological analysis not only is laborious but also does not allow for convenient reconstruction of the volumetric data,[6] which is preferred in most cases. Realizing the rich absorption contrasts

present in the biological samples after histochemical staining, we have successfully extended its application to PAM imaging of cells in 3D scaffolds without any need of physical sectioning.[58] As shown in Figure 5, a–c, after the MT3T3 cells in a PLGA inverse opal scaffold had been stained for f-actin sequentially with biotin-phalloidin, streptavidin-horseradish peroxidase (HRP), and diaminobenzidine (DAB) peroxidase substrate, they became readily visible under both conventional bright-field optical microscopy and OR-PAM. As expected, the optical microscope could only image the cells at the top surface of the scaffold and one had to section the scaffold into slices in order to observe the cells in the pores beneath (Fig. 5a). On the contrary, the stained cells in multiple layers of the pores in the scaffold were well discernible at single-cell resolution under OR-PAM (Fig. 5, b and c). The volumetric information gathered from PAM further allowed for optical sectioning of the scaffold and observation of the cells at any selected depth (Fig. 5c).

Interestingly, just like histological staining, PAM is also capable of imaging multiple cell types co-cultured in the same scaffold, thanks to the development of peroxidase substrates that generate precipitation products of different colors, such as ImmPACT™ DAB (brown), ImmPACT™ NovaRed/AEC (red), ImmPAC™ VIP (purple), and Vector® SG (blue/gray).[59] By taking advantages of the distinctive absorption spectra of these chromogenic agents, PAM can be used to achieve spectral un-mixing through scanning a sample at carefully chosen wavelengths. In one example, MC3T3 preosteoblasts and SK-BR-3 breast cancer cells were mixed and seeded onto an inverse opal scaffold, after which the cells underwent a dual-color staining procedure.[58] The f-actin of both types of cells was stained in brown with biotin-phalloidin, streptavidin-HRP, and DAB, whereas the human epidermal growth factor receptor 2 (HER2) on the surface of the SK-BR-3 cells were stained in red by biotin-anti-HER2 antibody, streptavidin-HRP, and the NovaRED peroxidase substrate. It was found that, the product of DAB/HRP had a distinct absorption peak centered at approximately 500 nm, with both products of DAB/HRP and NovaRED/HRP showing similar absorptions at >570 nm. Using a dual-wavelength scanning at 523 nm and 570 nm, PAM could digitally separate the two cell populations in the scaffold with individual SK-BR-3 cells distinguishable (Fig. 5, d and e). Spatial distribution of the SK-BR-3 cells across the entire MC3T3-coated scaffold was also available through the volumetric PAM data (Fig. 5e, bottom panel).

It was further shown that, the conventional histology methods relying on non-specific staining also power PAM imaging.[58] For example, hematoxylin and eosin (H&E) that stain cell nuclei blue and cytoplasm pink, respectively, allow for convenient PAM differentiation of the two subcellular components; the Masson's Trichrome staining that renders erythrocytes red, cytoplasm/muscle pinkish purple, and collagen blue endows PAM the capability to not only spectrally un-mix these components but also quantify their area percentages. In a sense, PAM has significantly increased the capacity of the conventional histology and immunohistochemistry by adding a third dimension to imaging the stained specimens. The volumetric imaging of absorption-rich biological structures provided by PAM essentially eliminates the need of physically sectioning, thus maintaining the integrity of the samples and simultaneously reducing the labor involved in the process.

Besides staining based on chemicals, cells have also been efficiently labeled by nanoparticles to enhance their contrasts for PAM imaging. For example, Emelianov and co-workers have demonstrated that human mesenchymal stem cells (hMSCs) could uptake Au nanoparticles when they were incubated together.[60] The labeled hMSCs were then longitudinally monitored using ultrasound-guided PAM imaging both *in vitro* in a hydrogel phantom and *in vivo* in a rat intramuscular hind limb model for up to 7 days. Similarly, we have demonstrated that Au nanocages (AuNCs) could also serve as a strong contrast-enhancing agent for PAM imaging owing to their large optical cross-sections.[61, 62] When hMSCs were labeled with AuNCs, they could be readily detected by PAM both *in vitro* and *in vivo*.[63] The homing of such labeled hMSCs to the tumor region in a mouse model was subsequently monitored *in vivo* using OR-PAM. It was found that the uptake of AuNCs by the hMSCs did not decrease the viability of the cells nor alter their differentiation potential into multiple lineages, indicating that these contrast agents are superb candidates for PAM tracking of cells.

PAM Imaging of Scaffolds

Scaffolds are equally important as the cellular components in engineering functional tissues since they not only provide structural/mechanical supports to mold the tissues but also constitute the substrates to incorporate bioactive molecules for residing cells or invading tissues to respond.[2-4] In fact, characterizing the tissue constructs has been focused on ways to image the cells and tissues, and rarely has it been reported for the assessment of the matrices in a non-invasive manner. With the development of imaging techniques, biomedical engineers are starting to adopt advanced imaging modalities for investigating the properties of the scaffolds instead of the conventional invasive mass loss assessments.[8] For example, using fluorescently labeled hydrogels composed of poly(ethylene glycol) (PEG)-dextran, Edelman and colleagues were able to follow the material loss of the same scaffolds by fluorescence imaging.[64] Nonetheless, this pure optical method inevitably presented a limited resolution at the millimeter scale, thus rendering the fine structures of the scaffold undiscernible. Alternative approaches relying on ultrasonic imaging[11] and X-ray CT[8, 12] have also been developed, but both of them suffer from insufficient resolution and/or contrast. Therefore, PAM, with an elegant combination of optical and ultrasonic imaging, has become an enabling modality to characterize the scaffolds.

Since most biomaterials themselves do not possess strong optical absorption, contrast mechanisms typically need to be incorporated into the scaffolds prior to PAM imaging. To this end, single-walled carbon nanotubes (SWCNTs) have been incorporated into PLGA inverse opal scaffolds to enhance their absorption contrast.[65, 66] Using OR-PAM, Wang, Sitharaman, and co-workers quantified the average porosity and pore size of the scaffolds at a 2.6-μm lateral resolution, whereas AR-PAM further extended the tissue penetration to deeper than 2 mm at slightly reduced resolution of 45 μm. Building upon this work, we have doped PLGA inverse opal scaffolds with the more biocompatible MTT formazan as a contrast agent, and investigated the degradation of such scaffolds with respect to two different media: phosphate buffered saline (PBS) and the more physiologically simulating body fluid, PBS supplemented with lipase. Using the OR-PAM, the fine structures of the scaffolds with a thickness of 2 mm could be clearly observed in depth-coded MAP images

(Fig. 6, a–d and e–h). As expected, when incubated in pure PBS without any supplements, the PLGA scaffold did not show signification alteration in morphology over the 6-week period tested (Fig. 6, a–d). In comparison, the scaffold immersed in a microenvironment containing lipase completely degraded by the end of 6 weeks (Fig. 6, e–h), indicating the cleavage of the ester unit in the PLGA backbone by the lipase. Magnified PAM images further revealed the superior resolution of the OR-PAM system, where individual pores and even the windows interconnecting adjacent pores in the scaffold were clearly visible (Fig. 6, i–l). AR-PAM was then used to quantitatively assess the degradation profiles of the scaffolds. It was found that the scaffolds degraded by 40% and 90%, respectively, in the two types of media as calculated from the PAM volumetric data. The quantification results obtained using PAM correlated well with those measured from similar scaffolds using the invasive mass loss assay. More recently, Pérez-Juste and co-workers doped poly(N-isopropylacrylamide) microgels with Au nanorods to significantly increase the absorption contrast of the hydrogel scaffolds, potentially rendering them visible under PAM.[67]

PAM Imaging of Vasculature

Blood vessels play a critical role in maintaining the viability and functionality of engineered tissues by transporting oxygen, nutrients, and wastes to and away from the tissues.[68] Nonetheless, it remains a challenge to non-invasively monitor and measure the development of the neovasculature inside the tissue constructs over time at high resolution and deep penetration. The most widely used imaging modalities for assessing the neovascularization process in implanted scaffolds include micro-CT[69] and confocal/two-photon microscopy.[70] Both of these modalities, require the administration of exogenous contrast agents, in addition to the ionizing irradiation caused by X-ray and the insufficient penetration depth offered by the optical methods. PAM, on the other hand, is well suited for performing this task. As discussed before, hemoglobin exhibits strong intrinsic optical absorption spanning across the entire UV-visible-NIR range,[7, 16, 17, 20, 26, 27, 33, 71] making it readily measurable by PAM.

We have demonstrated the capability of PAM to monitor the infiltration of blood vessels into 3D porous scaffolds.[72] We fabricated PLGA inverse opal scaffolds of two sets of uniform sizes, 200 μm and 80 μm, respectively, and implanted them in a mouse ear model. Using AR-PAM, we successfully monitored the development of neovasculature from the surrounding tissues into the same scaffolds without the need to sacrifice the animals, at single-vessel resolution and >3 mm imaging depth. Figure 7, a–d and e–h, shows PAM coronal/sagittal MAP images taken at Weeks 1, 2, 4, and 6 for the two types of scaffolds, respectively. By comparing the two groups of images, distinct patterns of neovascularization could be observed: the scaffold with larger pores induced higher degree of neovascularization than that with smaller pores, particularly at later stages of implantation. Such a difference could further be quantified using the PAM volumetric data, where the vessels in the scaffolds with 200-μm pores had more than twice total areas of those in the scaffolds with 80-μm pores (Fig. 7, i and j). Two parallel groups of animals bearing the same scaffolds were subjected to histology to measure the blood vessel ingrowth into the scaffolds, and the results obtained from these invasive assessments matched well with the non-invasive PAM quantifications (Fig. 7, i and j). Because of the optical sectioning

capability, the areas of infiltrating blood vessel at the surface *versus* the center of the two types of scaffolds could be further analyzed for the PAM data, which again, were similar to those calculated from the physical histology sections (Fig. 7k). In all quantification results, the area of blood vessels at each time point was normalized against that of the scaffold with a pore size of 80 μm at Week 2.

The PAM imaging of neovascularization in engineered tissues could potentially replace the conventional histology assays, especially when long-term monitoring of the same implants is needed. Indeed, the invasive histology analyses not only require sacrifice of multiple animals at each time point, but more labor-intensively involve additional sectioning and staining procedures to mark the blood vessels for subsequent measurements. The variations in the scaffolds themselves might potentially alter the pattern of neovascularization as well. By contrast, the few animals can be monitored longitudinally using PAM due to its non-invasive nature, rendering the analyses more accurate for the individual scaffolds of interest.

Interestingly, a number of groups have demonstrated that some lipids present in the vessel walls could also be detected using PAM or its macroscopic variants due to the absorption of these chemical species in the NIR region (approximately 1200–1800 nm).[73-76] The ability of PAM to image the lipid-rich plaques in blood vessels provides a convenient approach to non-invasive detection of vascular malfunctions such as arteriosclerosis and coronary artery diseases.

Probing Scaffold-Tissue Interactions with PAM

A rational extension of the applications of PAM in regenerative medicine discussed above should naturally converge to a stage where both the biological component and scaffold can be monitored simultaneously. This concept has spurred the utilization of PAM in probing the scaffold-tissue interactions in a non-invasive manner. By doping PLGA inverse opal scaffolds with MTT formazan, followed by implantation of the scaffolds in a mouse ear model, we could monitor the degradation of individual scaffolds *in vivo* by AR-PAM for weeks without sacrificing the animal (Fig. 8, a–d).[77] The main body of the scaffold reduced its size over time, with small pieces falling off, gradually disappearing, and being uptaken by the vasculature. It should be noted that, at the scanning wavelength of 638 nm, only the scaffold was visible while the interference from the blood vessels was minimized due to the relatively weaker absorption of hemoglobin compared to MTT formazan at this wavelength. The quantitative data derived from PAM imaging was similar to those obtained using the conventional destructive, mass-loss assessment (Fig. 8e), indicating the accuracy of the imaging approach. When switched to 578 nm, on the other hand, we were able to acquire images of both the scaffold and vasculature because both hemoglobin and MTT formazan have strong absorptions at this wavelength. After subtracting the signals from the scaffold, the blood vessel component could be singled out with a minimal interference from the scaffold. Figure 8, f–i, shows co-registered 3D depictions of the blood vessels (red) and the scaffold (green) at Weeks 0, 1, 3, and 6 post implantation. The degradation of the scaffold and the remodeling of blood vessels could be identified at the same time from these images. The corresponding cross-sectional images in Figure 8, j–m, further revealed the decrease in thickness and diameter for the scaffold with hints of infiltrating blood vessels into the

interior of the scaffold from the surrounding. The thickness of the scaffold decreased from about 1.5 mm at Week 0 to roughly 0.8 mm at Week 6, and some blood vessels were observed to develop into the void space of the scaffold.

PAM characterization of the scaffold-tissue interactions can also benefit from a multi-modality platform. For example, the aforementioned OR-PAM-FCM hybrid system[39] has been used to interrogate the behaviors of cells inside biomaterial scaffolds (unpublished data). When the scaffold is stained with a fluorescence probe such as rhodamine, it could be well resolved through the use of FCM subsystem (Fig. 9a). When seeded with melanoma cells, OR-PAM-FCM could be effectively used to monitor the proliferation and migration of cells in relation to the pores of the scaffold over a period of 7 days (Fig. 9, b and c).

The OR-PAM-OCT hybrid system is another great candidate.[40] While PAM images cells and tissues at high resolution and strong absorption contrast, the OCT subsystem, on the other hand, could resolve the structures of the polymeric scaffolds in a label-free manner due to the strong optical scattering contrast provided by the mismatching refractive indices of the biomaterial and the surrounding medium. Using OCT, it is unnecessary to further stain the scaffolds with exogenous contrast agents, thus minimizing potential modification to their properties caused by the doping process. In one demonstration, we cultured melanoma cells on a PLGA inverse opal scaffold and monitored the behaviors of the cells over a course of 6 days (unpublished data). As indicated in Figure 9d, the proliferation and inward migration of the melanoma cells could be observed using OR-PAM-OCT at a resolution of <5 μm. In addition, both the PAM and OCT subsystems could achieve a deep penetration depth of approximately 1 mm, spanning across the entire thickness of the scaffold (Fig. 9e). The volumetric data could also be 3D-rendered to reveal the spatial distribution of cells in the scaffold (Fig. 9f).

Furthermore, OR-PAM-OCT has been demonstrated for its capability in simultaneously imaging the vasculature and scaffold *in vivo*.[72] Figure 10, a–c and d–f, shows the development of vasculature in a mouse ear surrounding the implant and the morphological changes to the scaffold for 6 weeks. The arrowheads in Figure 10, d–f, indicate the expansion of the pores in the scaffold potentially due to its degradation. Superimposed cross-sectional images and 3D reconstruction views further revealed the invasion of blood vessels from the surface into the pores in the scaffold (Fig. 10, g–i), reaching a depth of >1 mm by the end of Week 6 (Fig. 10i).

Perspective

While a significant progress has been made in demonstrating the unique application of PAM for characterizing engineered tissue constructs, more systematic investigations are still needed before we can take full advantage of the functional imaging capacity of PAM. For example, interactions among multiple cell types inside a scaffold can be performed by genetically engineering the cells to express chromoproteins of different absorption spectra.[78] A step further, animals can be engineered to render specific cell populations with desired optical absorptions, allowing for direct observation of the host responses to an implant. Additionally, PAM can measure the flow rate (*via* the Doppler flowmetry[79]) and the

metabolic activity in blood (based on the differential absorption properties of oxyhemoglobin [HbO$_2$] and deoxyhemoglobin [Hb][26, 35, 71]) in a label-free manner, revealing not only the morphology but also the functions of the vasculature developed in the scaffolds. With further advancement in the instrumentation of PAM systems and integration with state-of-the-art sample preparation techniques (*e.g.*, CLARITY,[80] and expansion microscopy[81]), we believe that it will emerge as one of the standard imaging modalities for biomedical engineers who are particularly interested in applications related to regenerative medicine.

Acknowledgments

References

1. Langer R, Vacanti JP. Tissue engineering. Science. 1993; 260:920–926. [PubMed: 8493529]

2. Ma PX. Scaffolds for tissue fabrication. Mater Today. 2004; 7:30–40.

3. Zhang YS, Xia Y. Multiple facets for extracellular matrix mimicking in regenerative medicine. Nanomedicine. 2015; 10:689–692. [PubMed: 25816873]

4. Freed LE, Vunjak-Novakovic G, Biron RJ, Eagles DB, Lesnoy DC, Barlow SK, Langer R. Biodegradable polymer scaffolds for tissue engineering. Nat Biotechnol. 1994; 12:689–693.

5. Zhang YS, Choi SW, Xia Y. Inverse opal scaffolds for applications in regenerative medicine. Soft Matter. 2013; 9:9747–9754.

6. Song Y, Treanor D, Bulpitt AJ, Magee DR. 3d reconstruction of multiple stained histology images. J Pathol Inform. 4:2013.

7. Cai X, Zhang YS, Xia Y, Wang LV. Photoacoustic microscopy in tissue engineering. Mater Today. 2013; 16:67–77.

8. Appel AA, Anastasio MA, Larson JC, Brey EM. Imaging challenges in biomaterials and tissue engineering. Biomaterials. 2013; 34:6615–6630. [PubMed: 23768903]

9. Yuste R. Fluorescence microscopy today. Nat Methods. 2005; 2:902–904. [PubMed: 16299474]

10. Wang L, Jacques SL, Zheng L. MCML—Monte Carlo modeling of light transport in multi-layered tissues. Comput Methods Programs Biomed. 1995; 47:131–146. [PubMed: 7587160]

11. Kim K, Jeong CG, Hollister SJ. Non-invasive monitoring of tissue scaffold degradation using ultrasound elasticity imaging. Acta Biomater. 2008; 4:783–790. [PubMed: 18348913]

12. Appel A, Anastasio MA, Brey EM. Potential for imaging engineered tissues with x-ray phase contrast. Tissue Eng B. 2011; 17:321–330.

13. Peptan IA, Hong L, Xu H, Magin RL. Mr assessment of osteogenic differentiation in tissue-engineered constructs. Tissue Eng. 2006; 12:843–851. [PubMed: 16674297]

14. Del Guerra A, Belcari N. State-of-the-art of pet, spect and ct for small animal imaging. Nucl Instrum Methods Phys Res A. 2007; 583:119–124.

15. Wang X, Pang Y, Ku G, Xie X, Stoica G, Wang LV. Noninvasive laser-induced photoacoustic tomography for structural and functional in vivo imaging of the brain. Nat Biotechnol. 2003; 21:803–806. [PubMed: 12808463]

16. Zhang HF, Maslov K, Stoica G, Wang LV. Functional photoacoustic microscopy for high-resolution and noninvasive in vivo imaging. Nat Biotechnol. 2006; 24:848–851. [PubMed: 16823374]

17. Wang LV. Multiscale photoacoustic microscopy and computed tomography. Nat Photon. 2009; 3:503–509.

18. Ntziachristos V. Going deeper than microscopy: The optical imaging frontier in biology. Nat Methods. 2010; 7:603–614. [PubMed: 20676081]

19. Beard P. Biomedical photoacoustic imaging. Interface focus. 2011 rsfs20110028.

20. Wang LV, Hu S. Photoacoustic tomography: In vivo imaging from organelles to organs. Science. 2012; 335:1458–1462. [PubMed: 22442475]

21. Rajian JR, Li R, Wang P, Cheng JX. Vibrational photoacoustic tomography: Chemical imaging beyond the ballistic regime. J Phys Chem Lett. 2013; 4:3211–3215.

22. O'Donnell M, Wei CW, Xia J, Pelivanov I, Jia C, Huang SW, Hu X, Gao X. Can molecular imaging enable personalized diagnostics? An example using magnetomotive photoacoustic imaging. Ann Biomed Eng. 2013; 41:2237–2247. [PubMed: 23982280]

23. Taruttis A, Ntziachristos V. Advances in real-time multispectral optoacoustic imaging and its applications. Nat Photon. 2015; 9:219–227.

24. Zhang C, Maslov K, Wang LV. Subwavelength-resolution label-free photoacoustic microscopy of optical absorption in vivo. Opt Lett. 2010; 35:3195–3197. [PubMed: 20890331]

25. Wang Y, Maslov K, Zhang Y, Hu S, Yang L, Xia Y, Liu J, Wang LV. Fiber-laser-based photoacoustic microscopy and melanoma cell detection. J Biomed Opt. 2011; 16:011014–011014. [PubMed: 21280901]

26. Zhang HF, Maslov K, Sivaramakrishnan M, Stoica G, Wang LV. Imaging of hemoglobin oxygen saturation variations in single vessels in vivo using photoacoustic microscopy. Appl Phys Lett. 2007; 90:053901–053903.

27. Hu S, Maslov K, Wang LV. Second-generation optical-resolution photoacoustic microscopy with improved sensitivity and speed. Opt Lett. 2011; 36:1134–1136. [PubMed: 21479007]

28. Liu Y, Zhang C, Wang LV. Effects of light scattering on optical-resolution photoacoustic microscopy. J Biomed Opt. 2012; 17:126014–126014. [PubMed: 23232794]

29. Yao J, Wang LV. Photoacoustic microscopy. Laser Photon Rev. 2013; 7:758–778.

30. Durnin J, Eberly JH, Miceli JJ. Comparison of Bessel and Gaussian beams. Opt Lett. 1988; 13:79–80. [PubMed: 19741986]

31. Li ML, Zhang HF, Maslov K, Stoica G, Wang LV. Improved in vivo photoacoustic microscopy based on a virtual-detector concept. Opt Lett. 2006; 31:474–476. [PubMed: 16496891]

32. Liao CK, Li ML, Li PC. Optoacoustic imaging with synthetic aperture focusing and coherence weighting. Opt Lett. 2004; 29:2506–2508. [PubMed: 15584276]

33. Song KH, Wang LV. Deep reflection-mode photoacoustic imaging of biological tissue. J Biomed Opt. 2007; 12:060503–060503. [PubMed: 18163798]

34. Chatni MR, Xia J, Sohn R, Maslov K, Guo Z, Zhang Y, Wang K, Xia Y, Anastasio M, Arbeit J, Wang LV. Tumor glucose metabolism imaged in vivo in small animals with whole-body photoacoustic computed tomography. J Biomed Opt. 2012; 17:076012–076017. [PubMed: 22894495]

35. Yao J, Maslov KI, Zhang Y, Xia Y, Wang LV. Label-free oxygen-metabolic photoacoustic microscopy in vivo. J Biomed Opt. 2011; 16:076003–076011. [PubMed: 21806264]

36. Wang L, Maslov K, Wang LV. Single-cell label-free photoacoustic flowoxigraphy in vivo. Proct Natl Acad Sci USA. 2013; 110:5759–5764.

37. Favazza CP, Jassim O, Cornelius LA, Wang LV. In vivo photoacoustic microscopy of human cutaneous microvasculature and a nevus. J Biomed Opt. 16:016015-016015–016016. 2011. [PubMed: 21280921]

38. Kruger RA, Lam RB, Reinecke DR, Del Rio SP, Doyle RP. Photoacoustic angiography of the breast. Med Phys. 2010; 37:6096–6100. [PubMed: 21158321]

39. Wang Y, Hu S, Maslov K, Zhang Y, Xia Y, Wang LV. In vivo integrated photoacoustic and confocal microscopy of hemoglobin oxygen saturation and oxygen partial pressure. Opt Lett. 2011; 36:1029–1031. [PubMed: 21478972]

40. Li L, Maslov K, Ku G, Wang LV. Three-dimensional combined photoacoustic and optical coherence microscopy for in vivo microcirculation studies. Opt Express. 2009; 17:16450–16455. [PubMed: 19770860]

41. Kim C, Favazza C, Wang LV. In vivo photoacoustic tomography of chemicals: High-resolution functional and molecular optical imaging at new depths. Chem Rev. 2010; 110:2756–2782. [PubMed: 20210338]

42. Ntziachristos V, Razansky D. Molecular imaging by means of multispectral optoacoustic tomography (MSOT). Chem Rev. 2010; 110:2783–2794. [PubMed: 20387910]

43. Zhang Y, Cai X, Choi SW, Kim C, Wang LV, Xia Y. Chronic label-free volumetric photoacoustic microscopy of melanoma cells in three-dimensional porous scaffolds. Biomaterials. 2010; 31:8651–8658. [PubMed: 20727581]

44. Shaner NC, Steinbach PA, Tsien RY. A guide to choosing fluorescent proteins. Nat Methods. 2005; 2:905–909. [PubMed: 16299475]

45. Daniel R, Martin D, Claudio V, Rui M, Norbert P, Reinhard WK, Vasilis N. Multispectral opto-acoustic tomography of deep-seated fluorescent proteins in vivo. Nat Photonics. 2009; 3:412–417.

46. Filonov GS, Krumholz A, Xia J, Yao J, Wang LV, Verkhusha VV. Deep-tissue photoacoustic tomography of a genetically encoded near-infrared fluorescent probe. Angew Chem Int Ed. 2012; 51:1448–1451.

47. Krumholz A, Shcherbakova DM, Xia J, Wang LV, Verkhusha VV. Multicontrast photoacoustic in vivo imaging using near-infrared fluorescent proteins. Sci Rep. 4:2014.

48. Korner A, Pawelek J. Mammalian tyrosinase catalyzes three reactions in the biosynthesis of melanin. Science. 1982; 217:1163–1165. [PubMed: 6810464]

49. Krumholz A, Vanvickle-Chavez SJ, Yao J, Fleming TP, Gillanders WE, Wang LV. Photoacoustic microscopy of tyrosinase reporter gene in vivo. J Biomed Opt. 2011; 16:080503–080503. [PubMed: 21895303]

50. Jathoul AP, Laufer J, Ogunlade O, Treeby B, Cox B, Zhang E, Johnson P, Pizzey AR, Philip B, Marafioti T, Lythgoe MF, Pedley RB, Pule MA, Beard P. Deep in vivo photoacoustic imaging of mammalian tissues using a tyrosinase-based genetic reporter. Nat Photon. 2015; 9:239–246.

51. Mansour SL, Thomas KR, Deng CX, Capecchi MR. Introduction of a lacZ reporter gene into the mouse int-2 locus by homologous recombination. Proct Natl Acad Sci USA. 1990; 87:7688–7692.

52. Horwitz JP, Chua J, Curby RJ, Tomson AJ, Da Rooge MA, Fisher BE, Mauricio J, Klundt I. Substrates for cytochemical demonstration of enzyme activity. I. Some substituted 3-indolyl-β-d-glycopyranosides. J Med Chem. 1964; 7:574–575. [PubMed: 14221156]

53. Li L, Zemp RJ, Lungu G, Stoica G, Wang LV. Photoacoustic imaging of lacZ gene expression in vivo. J Biomed Opt. 2007; 12:020504–020504. [PubMed: 17477703]

54. Li L, Zhang HF, Zemp RJ, Maslov K, Wang LV. Simultaneous imaging of a lacZ-marked tumor and microvasculature morphology in vivo by dual-wavelength photoacoustic microscopy. J Innov Opt Health Sci. 2008; 1:207–215. [PubMed: 19946613]

55. Cai X, Li L, Krumholz A, Guo Z, Erpelding TN, Zhang C, Zhang Y, Xia Y, Wang LV. Multi-scale molecular photoacoustic tomography of gene expression. PLoS One. 2012; 7:e43999. [PubMed: 22952846]

56. Zhang Y, Cai X, Wang Y, Zhang C, Li L, Choi SW, Wang LV, Xia Y. Noninvasive photoacoustic microscopy of living cells in two and three dimensions through enhancement by a metabolite dye. Angew Chem Int Ed. 2011; 50:7359–7363.

57. Seidler E. The tetrazolium-fomazan system: Design and histochemistry. Prog Histochem Cytochem. 1991; 24:III–79.

58. Zhang YS, Yao JJ, Zhang C, Li L, Wang LHV, Xia YN. Optical-resolution photoacoustic microscopy for volumetric and spectral analysis of histological and immunochemical samples. Angew Chemie Int Ed. 2014; 53:8099–8103.

59. Discovery through color -- a guide to multiple antigen labeling. Burlingame: Vector Laboratories; 2005.

60. Nam SY, Ricles LM, Suggs LJ, Emelianov SY. In vivo ultrasound and photoacoustic monitoring of mesenchymal stem cells labeled with gold nanotracers. PLoS One. 2012; 7:e37267. [PubMed: 22615959]

61. Cho EC, Kim C, Zhou F, Cobley CM, Song KH, Chen J, Li ZY, Wang LV, Xia Y. Measuring the optical absorption cross sections of au-ag nanocages and au nanorods by photoacoustic imaging. J Phys Chem C. 2009; 113:9023–9028.

62. Xia Y, Li W, Cobley CM, Chen J, Xia X, Zhang Q, Yang M, Cho EC, Brown PK. Gold nanocages: From synthesis to theranostic applications. Acc Chem Res. 2011; 44:914–924. [PubMed: 21528889]

63. Zhang Y, Wang Y, Wang L, Wang Y, Cai X, Zhang C, Wang LV, Xia Y. Labeling human mesenchymal stem cells with au nanocages for in vitro and in vivo tracking by two-photon microscopy and photoacoustic microscopy. Theranostics. 2013; 3:532–543. [PubMed: 23946820]

64. Artzi N, Oliva N, Puron C, Shitreet S, Artzi S, Bon Ramos A, Groothuis A, Sahagian G, Edelman ER. In vivo and in vitro tracking of erosion in biodegradable materials using non-invasive fluorescence imaging. Nat Mater. 2011; 10:704–709. [PubMed: 21857678]

65. Cai X, Paratala BS, Hu S, Sitharaman B, Wang LV. Multiscale photoacoustic microscopy of single-walled carbon nanotube-incorporated tissue engineering scaffolds. Tissue Eng C. 2012; 18:310–317.

66. Talukdar Y, Avti P, Sun J, Sitharaman B. Multimodal ultrasound-photoacoustic imaging of tissue engineering scaffolds and blood oxygen saturation in and around the scaffolds. Tissue Eng C. 2014; 20:440–449.

67. FernáNdez-LoóPez C, Polavarapu L, Solís DM, Taboada JM, Obelleiro F, Contreras-CáCeres R, Pastoriza-Santos I, PéRez-Juste J. Gold nanorod–pnipam hybrids with reversible plasmon coupling: Synthesis, modeling, and sers properties. ACS Appl Mater Interfaces. 2015

68. Bae H, Puranik AS, Gauvin R, Edalat F, Carrillo-Conde B, Peppas NA, Khademhosseini A. Building vascular networks. Sci Transl Med. 2012; 4:160ps123–160ps123.

69. Phelps EA, Landázuri N, Thulé PM, Taylor WR, García AJ. Bioartificial matrices for therapeutic vascularization. Proct Natl Acad Sci USA. 2009

70. Spencer JA, Ferraro F, Roussakis E, Klein A, Wu J, Runnels JM, Zaher W, Mortensen LJ, Alt C, Turcotte R. Direct measurement of local oxygen concentration in the bone marrow of live animals. Nature. 2014; 508:269–273. [PubMed: 24590072]

71. Gottschalk S, Fehm TF, Deán-Ben XL, Razansky D. Noninvasive real-time visualization of multiple cerebral hemodynamic parameters in whole mouse brains using five-dimensional optoacoustic tomography. J Cereb Blood Flow Metab. 2015

72. Cai X, Zhang Y, Li L, Choi SW, Macewan MR, Yao J, Kim C, Xia Y, Wang LV. Investigation of neovascularization in 3d porous scaffolds in vivo by photoacoustic microscopy and optical coherence tomography. Tissue Eng C. 2013; 19:196–204.

73. Allen TJ, Hall A, Dhillon AP, Owen JS, Beard PC. Spectroscopic photoacoustic imaging of lipid-rich plaques in the human aorta in the 740 to 1400 nm wavelength range. J Biomed Opt. 2012; 17:0612091–06120910.

74. Wang B, Karpiouk A, Yeager D, Amirian J, Litovsky S, Smalling R, Emelianov S. Intravascular photoacoustic imaging of lipid in atherosclerotic plaques in the presence of luminal blood. Opt Lett. 2012; 37:1244–1246. [PubMed: 22466209]

75. Jansen K, Van Der Steen AFW, Wu M, Van Beusekom HMM, Springeling G, Li X, Zhou Q, Kirk Shung K, De Kleijn DPV, Van Soest G. Spectroscopic intravascular photoacoustic imaging of lipids in atherosclerosis. J Biomed Opt. 2014; 19:026006–026006. [PubMed: 24522806]

76. Wang P, Ma T, Slipchenko MN, Liang S, Hui J, Shung KK, Roy S, Sturek M, Zhou Q, Chen Z, Cheng JX. High-speed intravascular photoacoustic imaging of lipid-laden atherosclerotic plaque enabled by a 2-khz barium nitrite Raman laser. Sci Rep. 2014; 4:6889. [PubMed: 25366991]

77. Zhang Y, Cai X, Yao J, Wang LV, Xia Y. Non-invasive and in situ characterization of the degradation of biomaterial scaffolds by photoacoustic microscopy. Angew Chem Int Ed. 2014; 53:184–188.

78. Laufer J, Jathoul A, Pule M, Beard P. In vitro characterization of genetically expressed absorbing proteins using photoacoustic spectroscopy. Biomed Opt Express. 2013; 4:2477–2490. [PubMed: 24298408]

79. Brunker J, Beard P. Pulsed photoacoustic doppler flowmetry using time-domain cross-correlation: Accuracy, resolution and scalability. J Acoust Soc Am. 2012; 132:1780–1791. [PubMed: 22978905]

80. Chung K, Wallace J, Kim SY, Kalyanasundaram S, Andalman AS, Davidson TJ, Mirzabekov JJ, Zalocusky KA, Mattis J, Denisin AK. Structural and molecular interrogation of intact biological systems. Nature. 2013; 497:332–337. [PubMed: 23575631]

81. Chen F, Tillberg PW, Boyden ES. Expansion microscopy. Science. 2015; 347:1260088.
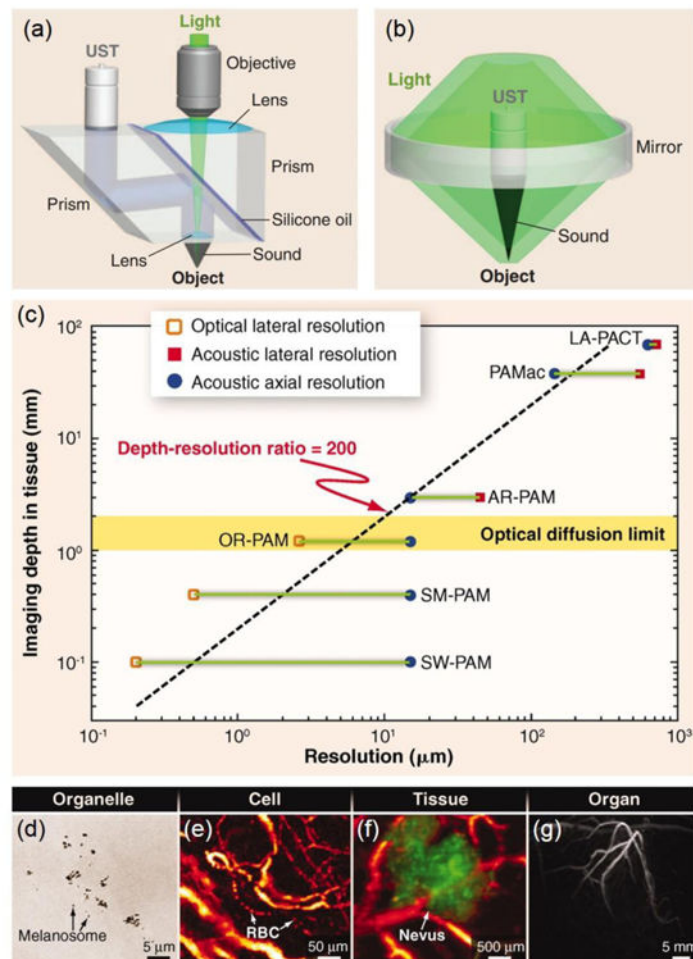
Figure 1.
(a, b) Schematic illustrations of (a) OR-PAM and (b) AR-PAM, respectively. (c) Imaging depth *versus* spatial resolution for PAM. SM, submicrometer; LA, linear array. (d–g) Multi-scale PAM images of organelles, cells, tissues, and organs *in vivo*: (d) subwavelength PAM of melanosomes in the ear of a black mouse; (e) OR-PAM of individual red blood cells traveling along a capillary in a mouse ear; (f) AR-PAM of a nevus on a human forearm; and (g) PACT of vasculature in a human breast. Adapted with permission from Ref.[20], copyright 2012 American Association for the Advancement of Science.
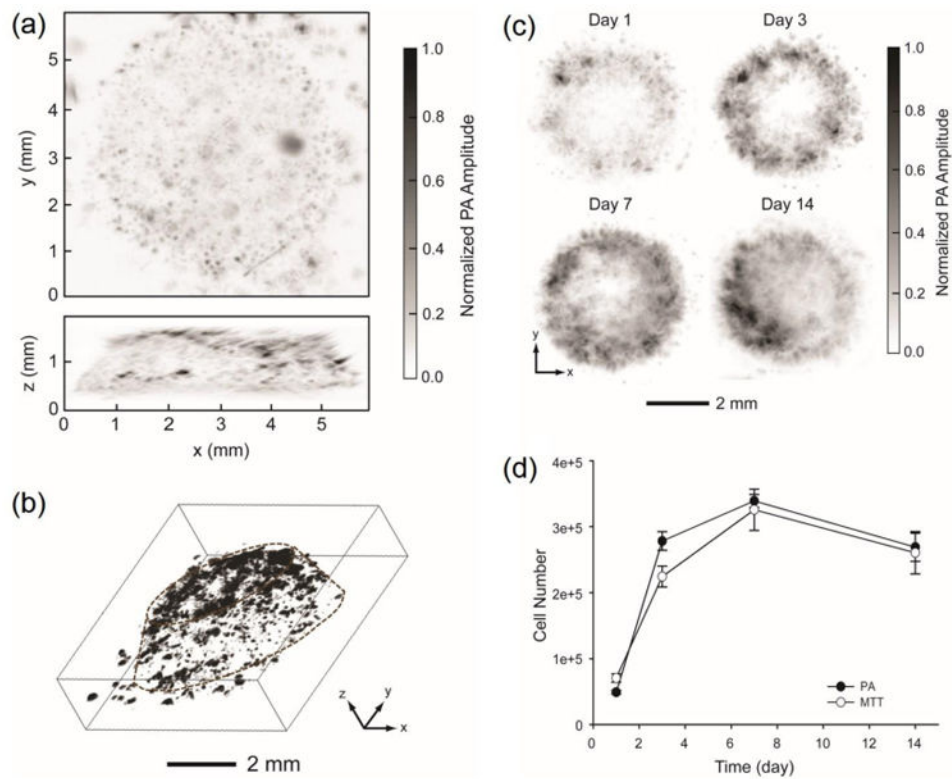
Figure 2.
(a) PAM coronal (top) and sagittal (side) MAP images. The black dots or patches correspond to melanoma cells. (b) A 3D reconstruction image, where the contour of the scaffold is marked by dotted lines. (c) Time course PAM images (coronal MAP of the entire volume) of melanoma cells in a typical PLGA inverse opal scaffold at 1, 3, 7, and 14 days post-seeding. (d) Quantitative analysis of melanoma cells in scaffolds derived from both the PAM volumetric data and the MTT assay. Adapted with permission from Ref.[43], copyright 2010 Elsevier.
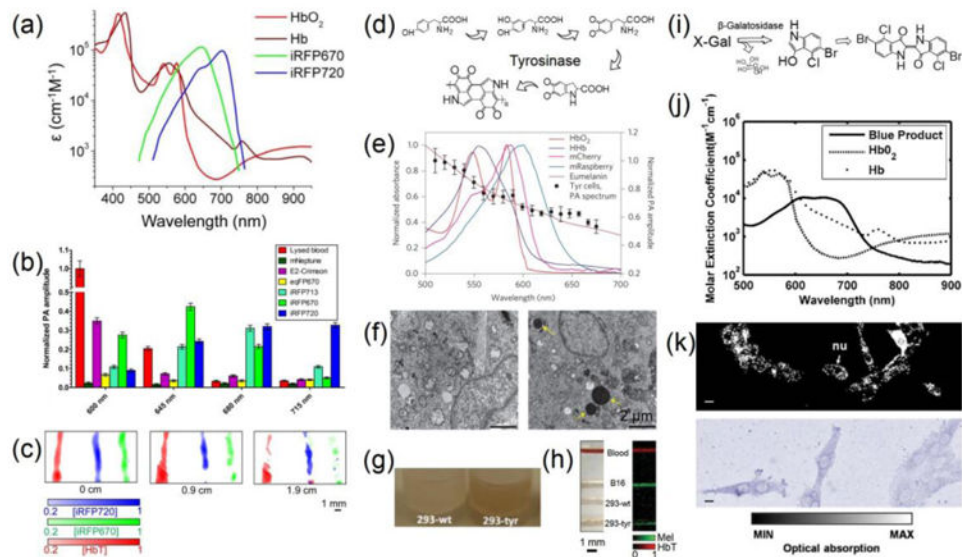
Figure 3.
(a) Overlay of the molar extinction spectra of iRFP670, iRFP720, HbO$_2$, and Hb. (b) Photoacoustic signal amplitudes of equal amounts of purified fluorescent proteins (mNeptune, E2-Crimson, eqRFP670, iRFP670, iRFP713, iRFP720) at the four indicated wavelengths. (c) PAM images of tubes containing lysed blood and equal concentrations of purified iRFP670 and iRFP720, unmixed at different depths (0, 0.9, and 1.9 mm) of overlaid tissue. Adapted with permission from Ref.[47], copyright 2014 Nature Publishing Group. (d) Schematic showing tyrosinase-induced melanin synthesis pathway. (e) Photoacoustic spectroscopy of tyrosinase (Tyr)-expressing cells. (c) Pigmented cytoplasmic granules in cells expressing Tyr observed by TEM: native (left) and Tyr-expressing cells (right). Adapted with permission from Ref.[50], copyright 2014 Nature Publishing Group. (g) Photograph of melanin production in wild-type (293-wt), and Try-transfected (293-TYR) cells. (h) Photograph and normalized photoacoustic results of tube phantom showing blood in red and melanin in green. Adapted with permission from Ref.[49], copyright 2011 International Society for Optics and Photonics. (i) Schematic diagram showing the X-gal/ galactosidase reaction. (j) Comparison of absorption spectra for the blue product, HbO$_2$, and Hb. Adapted with permission from Ref.[53], copyright 2007 International Society for Optics and Photonics. (k) OR-PAM MAP image and photograph showing 9L/lacZ cells stained with X-gal. nu: cell nucleus. Scale bars: 10 μm. Adapted with permission from Ref.[55], copyright 2012 Public Library of Science.
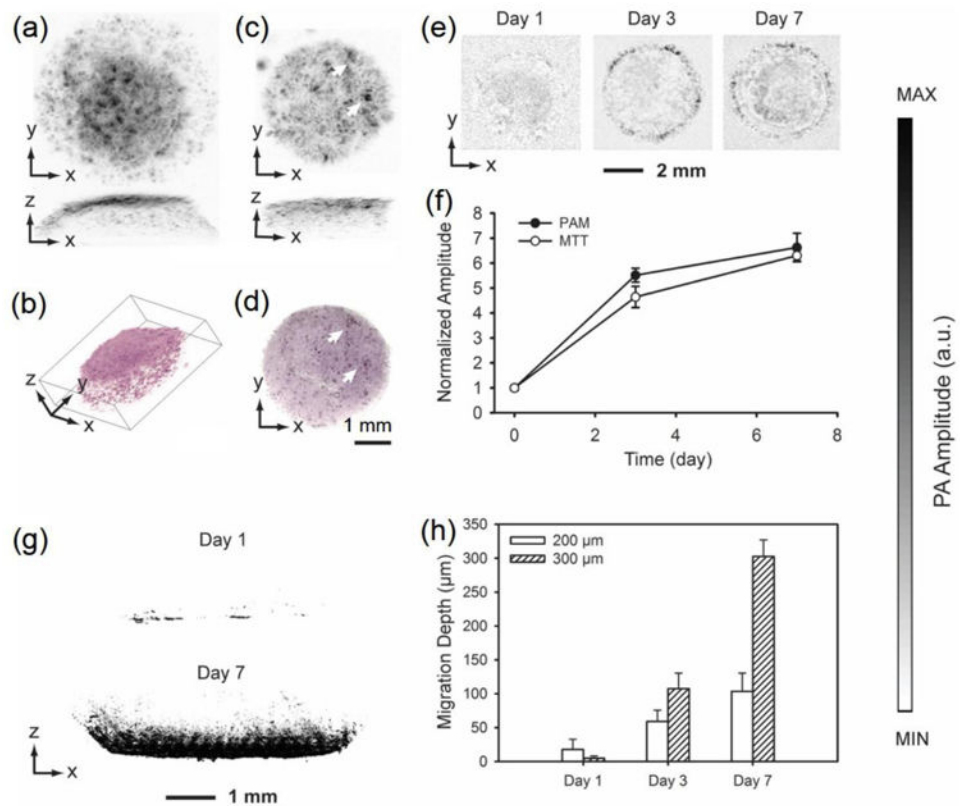
Figure 4.
(a) PAM MAP image of fibroblasts cultured in an inverse opal scaffold, followed by MTT staining; (b) 3D rendering of the volumetric PAM data in (a). (c) PAM MAP image of fibroblasts cultured in an inverse opal scaffold filled with cross-linked alginate hydrogel, followed by incubation with MTT; (d) an optical micrograph showing the same scaffold as in (c). The arrows indicate the matching features in PAM and optical microscopy. (e) PAM chronological images of fibroblasts grown in inverse opal scaffolds at 6 h, 3 days, and 7 days; (f) quantification of cell numbers in the scaffolds as determined by volumetric PAM data and parallel MTT biochemical assays. (g) PAM sagittal MAP images showing cell invasion profiles at Days 1 and 7 into inverse opal scaffolds with a pore size of 300 μm; (h) quantification of average cell penetration depths in scaffolds with pore sizes of 200 and 300 μm, respectively, as determined by PAM virtual biopsy. Adapted with permission from Ref.[56], copyright 2011 Wiley-VCH.
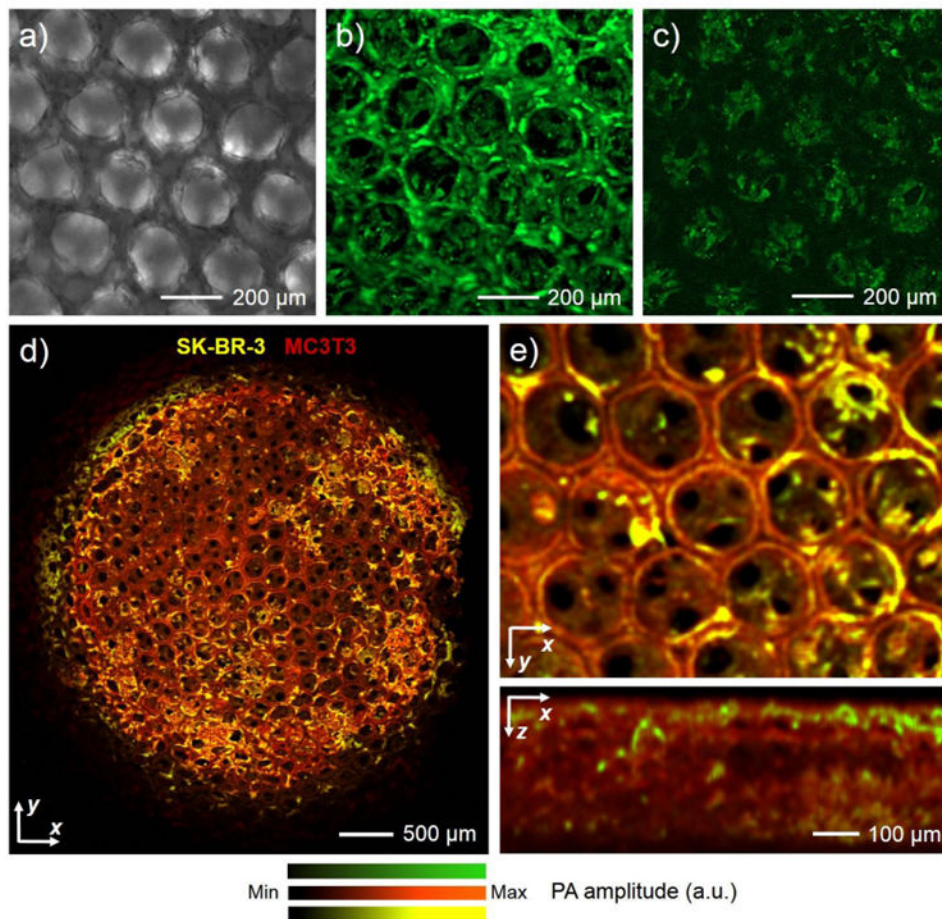
Figure 5.
(a) A transmission optical micrograph showing the cells cultured in an inverse opal scaffold for 3 days and stained with biotin-phalloidin/HRP-streptavidin/DAB. (b) OR-PAM MAP image of the same cell/scaffold construct in (a). (c) OR-PAM image showing the bottom section (100–200 μm beneath the top surface) of the surface pores in the scaffold. (d) OR-PAM MAP image of a co-culture of SK-BR-3 (stained for HER2 antigen with HRP/NovaRed) and MC3T3 preosteoblasts (stained for f-actin with HRP/DAB), where the two cell types could be digitally separated in the image using spectral un-mixing. (e) Magnified views of the same sample showing volumetric distribution of the two cell types from the top and side, respectively. Reprinted with permission from Ref.[58], copyright 2014 Wiley-VCH.
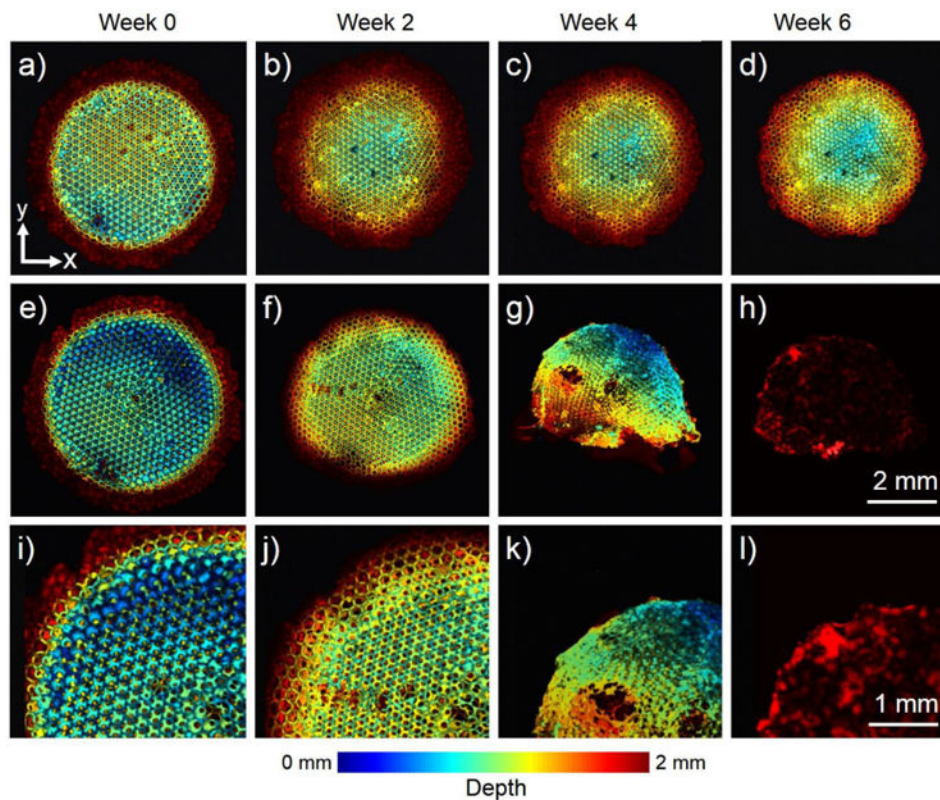
Figure 6.
(a–h) OR-PAM coronal projection images showing the degradation of a PLGA inverse opal scaffold immersed in (a–d) plain PBS and (e–h) PBS containing 0.025 wt.% lipase at 37 °C for a period up to 6 weeks. (i–l) Magnified views showing the top-left corner of the images in (e– h), respectively. While the scaffold in PBS did not undergo obvious structural alterations for up to Week 6, the scaffold showed remarkable changes over time in the presence of lipase. The images are color-coded by depth of maximum. Reprinted with permission from Ref.[77], copyright 2014 Wiley-VCH.
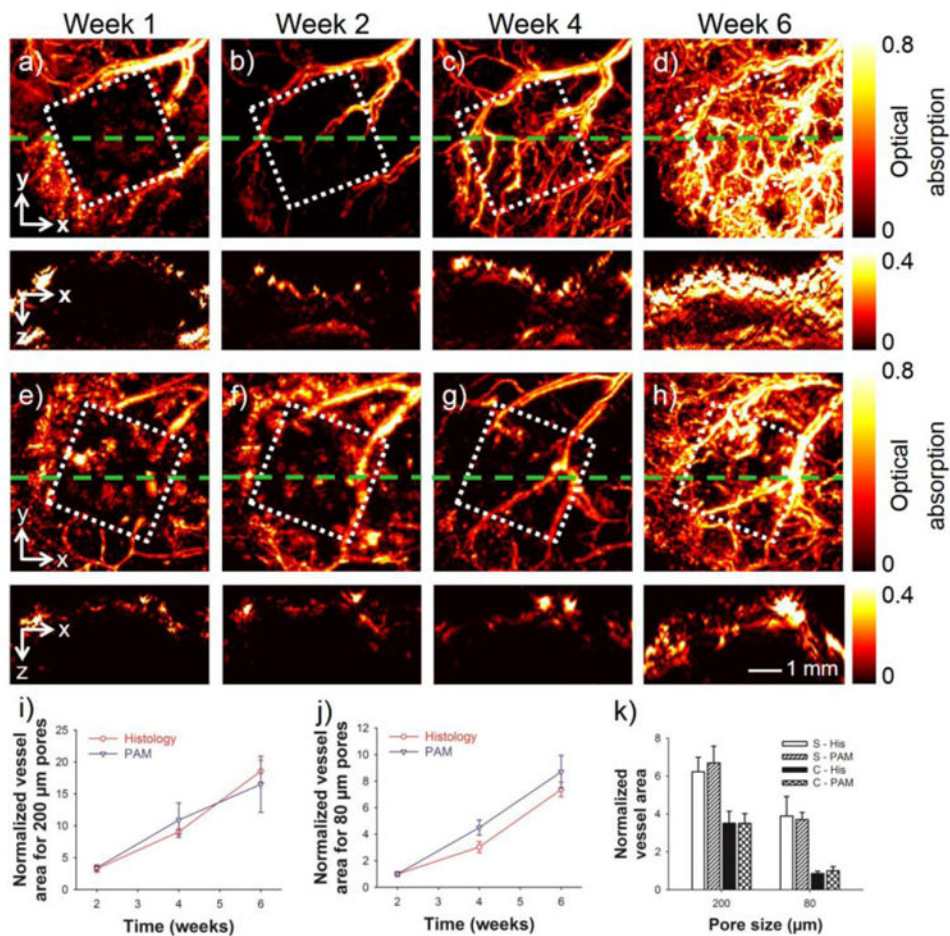
Figure 7.
(a–d) Top panel: MAP images showing the remodeling of neovasculature in a scaffold with a pore size of 200 μm at 1, 2, 4, and 6 weeks post implantation in a mouse ear model. Bottom panel: the corresponding cross-sectional images at planes marked by the green dashed lines. (e–h) Top panel: MAP images showing the remodeling of neovasculature in a scaffold with a pore size of 80 μm at 1, 2, 4, and 6 weeks post-implantation. Bottom panel: the corresponding cross-sectional images at planes marked by the green dashed lines. The square indicates the area where the scaffold resided. (i, j) Normalized blood vessel area calculated from both PAM data and histology for scaffolds with pore sizes of 200 μm and 80 μm, respectively. (k) Comparison of the blood vessel area in the scaffolds at planes close to the surface and in the central region of the scaffolds at 6 weeks post implantation. S: surface; C: center; His: histology. In (i–k) the area of blood vessels at each time point was normalized against that of the scaffold with a pore size of 80 μm at week 2. Reprinted with permission from Ref.[72], copyright 2011 Mary Ann Liebert, Inc.
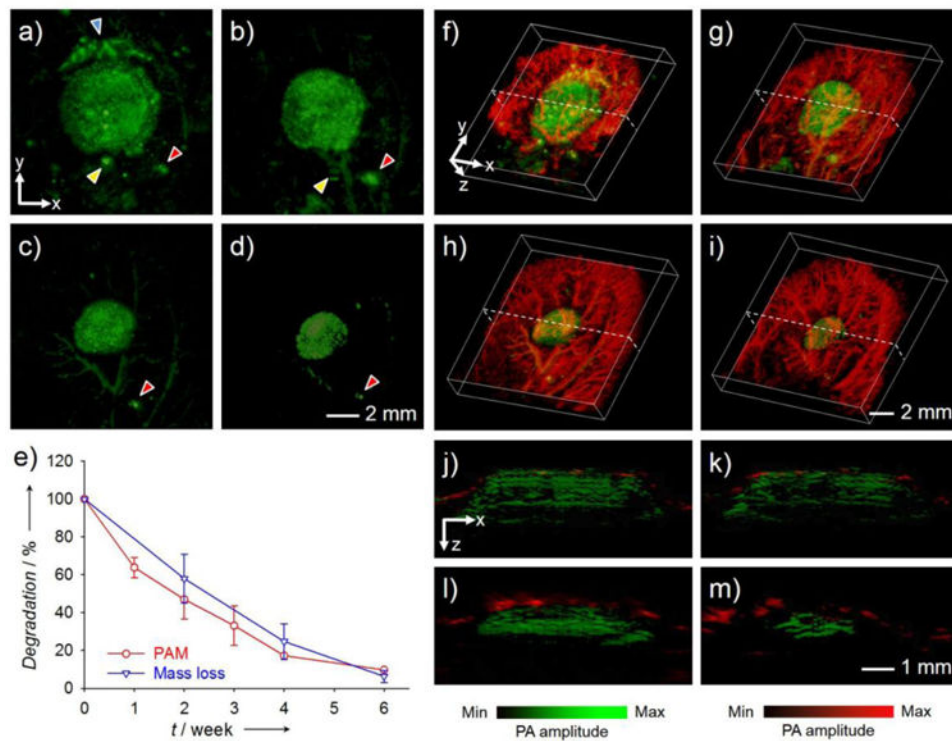
Figure 8.
(a–d) AR-PAM coronal MAP images taken from the same PLGA inverse opal scaffold implanted in the ear of a nude mouse at weeks 0, 1, 3, and 6 post implantation, respectively. The arrowheads indicate small pieces of the scaffold that likely came off during the surgery, and their slight changes in position and orientation relative to the main scaffold at different time points could be attributed to the activity of the mouse. (e) Comparison of the degradation profiles of scaffolds as a function of time obtained from the same scaffold using PAM and from different scaffolds using the conventional invasive mass loss assay. (f–i) Co-registered 3D reconstruction images showing both the degradation of the same scaffold and the remodeling of vasculature simultaneously. (j–m) Co-registered B-scan images at the dotted planes as indicated in (f–i), respectively. Reprinted with permission from Ref.[77], copyright 2014 Wiley-VCH.
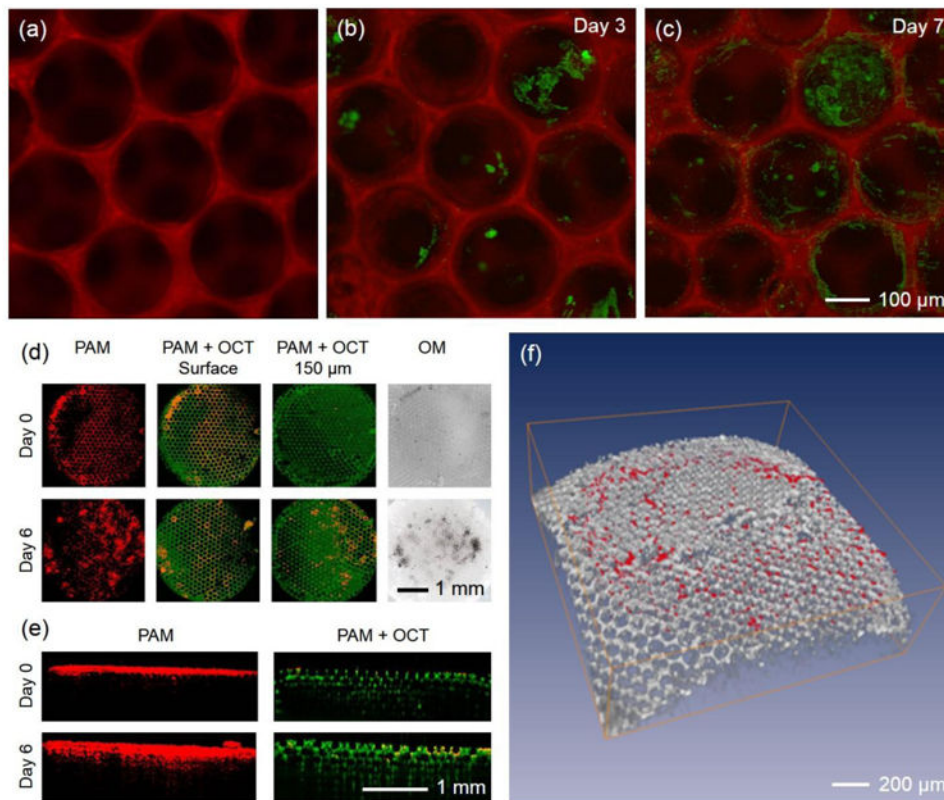
Figure 9.
(a) FCM imaging of a fluorescently labeled PLGA inverse opal scaffold using an OR-PAM-FCM hybrid system. (b, c) OR-PAM-FCM monitoring of melanoma cells grown on the scaffold, where the cells and scaffold were imaged using the PAM and FCM subsystems, respectively. OR-PAM-OCT images of melanoma cells cultured on an individual PLGA inverse opal scaffold for up to 6 days. (d, e) Coronal and sagittal views of the PAM and PAM/OCT images showing the ingrowth of melanoma cells from the surface into the center of the scaffold using the OR-PAM-OCT hybrid system. The melanoma cells were imaged by the PAM subsystem whereas the scaffold by the OCT subsystem in a label-free manner. (f) Volumetric rendering of the OCT-imaged scaffold (gray) with PAM-detected melanoma cells (red).
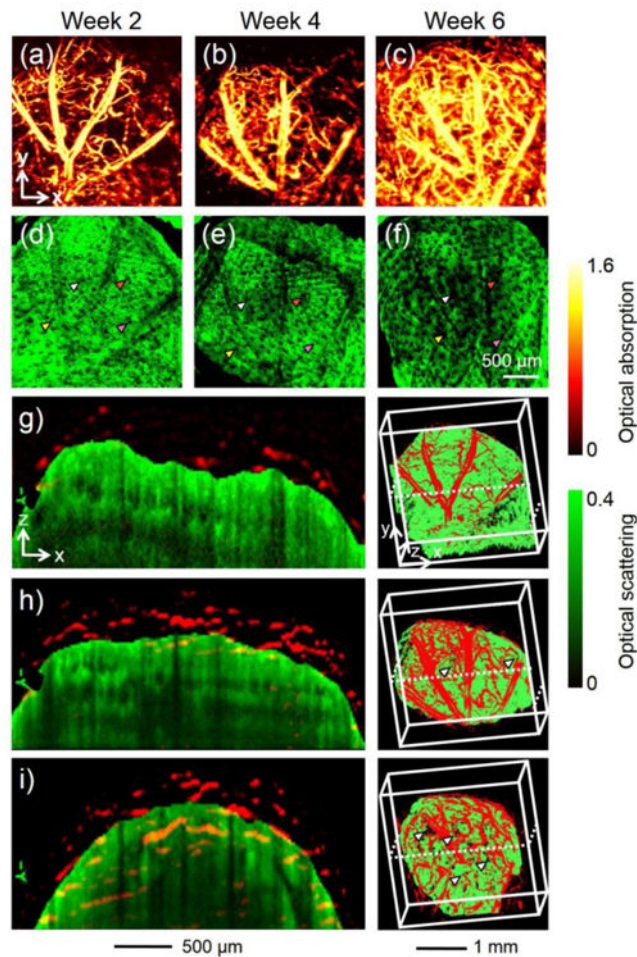
Figure 10.
(a–c) MAP PAM images showing the development of blood vessels into an inverse opal scaffold with a pore size of 200 μm at 2, 4, and 6 weeks, respectively, post implantation in a mouse ear model. (d–f) The corresponding OCT MAP images showing the scaffold/tissue construct. The signals from the skin layer were removed from all the OCT images to show the surface of the scaffold more clearly. Arrowheads indicate examples of local increase in pore size over time due to degradation of the scaffold. (g–i) Co-registered cross-sectional views and 3D depictions of the vasculature (red) and scaffold/tissue construct (green) at 2, 4, and 6 weeks, respectively, post-implantation. The arrowheads indicate the growth of neovasculature into the pores of the scaffold. Reprinted with permission from Ref.[72], copyright 2011 Mary Ann Liebert, Inc.